

# Tailoring Ni–Co–Mn–Sn Ribbons by Ge Doping for Enhanced Magnetocaloric Effect

Ali Ghotbi Varzaneh, Parviz Kameli, Mariana Ríos, Bagher Aslibeiki, Iñaki Orue, Tapati Sarkar, Volodymyr Chernenko, Manfred Kohl, Jingyuan Xu,\* and Daniel Salazar

Micro-grained high surface-to-volume ratio thin ribbons of magnetic shape memory  $\text{Ni}_{42}\text{Co}_8\text{Mn}_{39}\text{Sn}_{11-x}\text{Ge}_x$  ( $x = 1, 2, 3$ ) alloys are prepared, and their martensitic transformation (MT) behavior, magnetic and magnetocaloric properties are investigated. X-ray diffraction reveals that the incorporation of Ge consistently decreases the lattice parameters and the transformation volume change, thereby improving geometric compatibility between martensitic and austenitic crystal lattices. This improvement facilitated a reduction of the thermal hysteresis of MT to a minimum of  $\approx 12.1$  K at the Ge concentration of  $x = 2$ . Direct measurements of adiabatic temperature changes show that the  $x = 2$  alloy (SnGe2 ribbon) exhibited the highest peak value ( $\approx 2$  K) at a moderate magnetic field change of 1.96 T. In addition, SnGe2 ribbon demonstrates exceptional isothermal entropy changes of  $\Delta S_{iso} = 35.5$  J kg<sup>-1</sup> K<sup>-1</sup> K at 7 T and 22.8 J kg<sup>-1</sup> K<sup>-1</sup> K at 2 T, which are competitive with those of bulk alloys and surpassing previously reported melt-spun ribbons of the Heusler-type magnetocaloric materials. The significance of intricate microstructure in boosting the magnetocaloric effect is emphasized. These results highlight the substantial potential of Ni–Co–Mn–Sn–Ge thin ribbons as highly effective, micro-sized magnetocaloric materials for cutting-edge solid-state refrigeration systems.

## 1. Introduction

Magnetocaloric materials are regarded as the most promising options for solid-state refrigeration systems due to their energy-saving properties and environmental friendliness. Among them, Heusler-type magnetic shape memory alloys (MSMAs), particularly those based on Ni–Mn–Z (Z = In, Sn, Sb), exhibit a giant magnetocaloric effect (MCE) associated with a first-order magnetostructural transformation occurring near room temperature<sup>[1–3]</sup> This martensitic transformation (MT), from a weakly magnetic martensitic phase to a ferromagnetic austenite, is characterized by a strong magnetostructural coupling, that allows for a field-induced MT and inverse MCE.<sup>[4]</sup>

Despite high potential of these materials, several obstacles, such as significant thermal hysteresis, irreversibility, and the delicate balance between the change in


A. G. Varzaneh, M. Kohl, J. Xu  
Institute of Microstructure Technology  
Karlsruhe Institute of Technology  
76344 Karlsruhe, Germany  
E-mail: [jingyuan.xu@kit.edu](mailto:jingyuan.xu@kit.edu)

P. Kameli  
Department of Physics  
Isfahan University of Technology  
Isfahan 84156-83111, Iran  
M. Ríos, V. Chernenko, D. Salazar  
BCMaterials  
Basque Center for Materials  
Applications and Nanostructures  
EHU Science Park  
Leioa 48940, Spain

B. Aslibeiki  
Faculty of Physics  
University of Tabriz  
Tabriz, Iran

B. Aslibeiki, T. Sarkar  
Division of Solid State Physics  
Department of Materials Science and Engineering  
Uppsala University  
Uppsala SE-751 03, Sweden

I. Orue  
SGiker  
Vicerrectorado de Inv. UPV/EHU  
Leioa 48940, Spain  
V. Chernenko  
Ikerbasque  
Basque Foundation for Science  
Bilbao 48009, Spain

 The ORCID identification number(s) for the author(s) of this article can be found under <https://doi.org/10.1002/aelm.202500596>

© 2025 The Author(s). Advanced Electronic Materials published by Wiley-VCH GmbH. This is an open access article under the terms of the [Creative Commons Attribution](https://creativecommons.org/licenses/by/4.0/) License, which permits use, distribution and reproduction in any medium, provided the original work is properly cited.

DOI: 10.1002/aelm.202500596

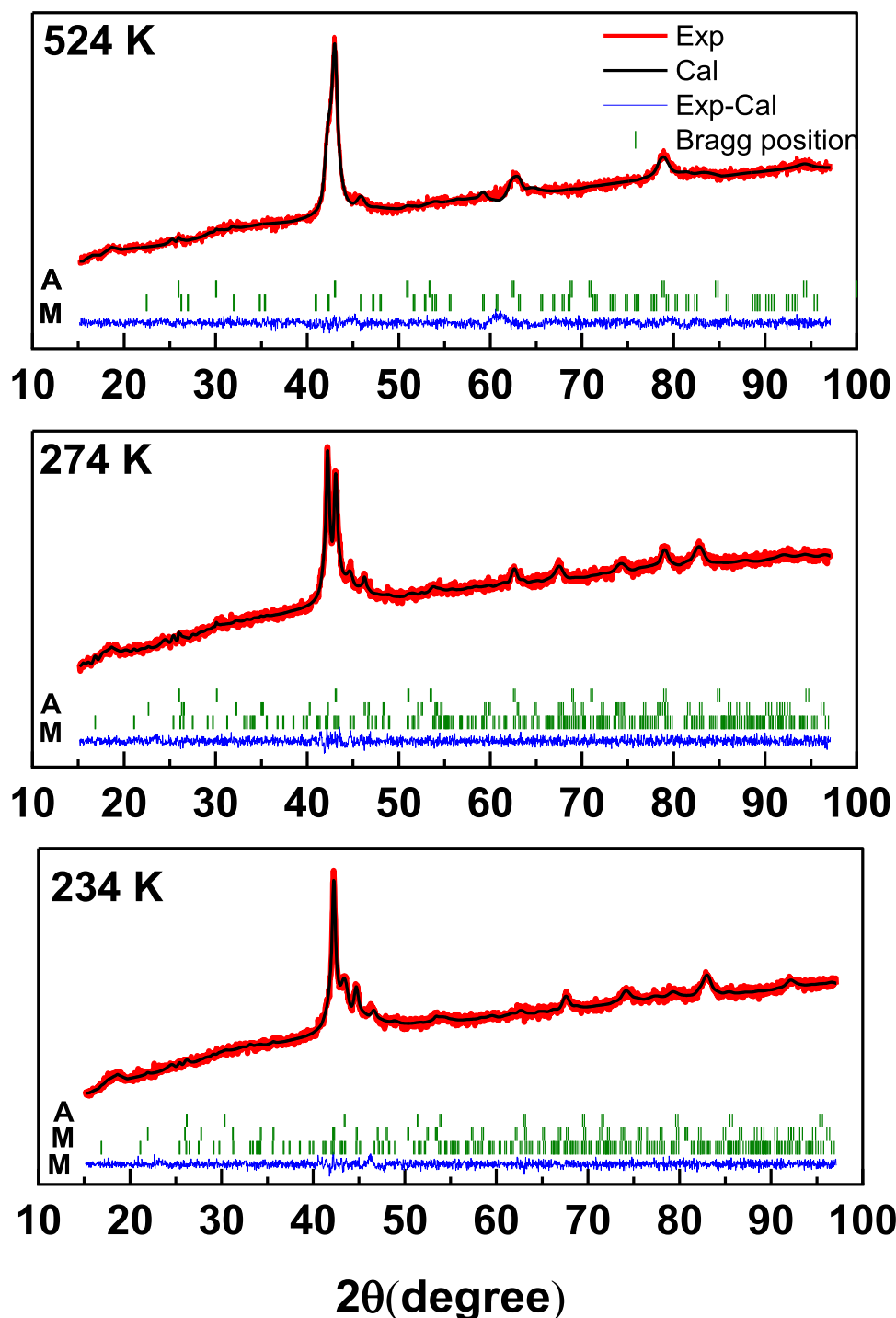


**Figure 1.** Representative X-ray diffraction patterns and results of the Rietveld refinement for the SnGe<sub>2</sub> ribbon at three temperatures: 524, 274, and 234 K. Letters A and M indicate the Bragg peak positions of the austenitic and martensitic phases, respectively.

magnetization ( $\Delta M$ ) and the total entropy change ( $\Delta S_t$ ) hinder the practical use of magnetocaloric materials.<sup>[1]</sup>

The incorporation of Co into quaternary Ni-Co-Mn-Sn alloys has been found to boost the  $\Delta M$  and enhance the ferromagnetic properties of the austenite phase.<sup>[5–7]</sup> However, as Gottschall et al. pointed out, while an increase in  $\Delta M$  is crucial for the mag-

netocaloric effect, it also leads to a rise in the opposing magnetic entropy, which can limit the overall caloric efficiency. This underscores the importance of fine-tuning  $\Delta M$  to maximize performance.<sup>[1]</sup>

Ge substitution for Sn has gained interest due to its intriguing impact on the MT temperatures. Although Ge and Sn have the

same electron configuration, their substitution results in unexpected alterations that cannot be fully accounted for by the well-established rule of electron concentration per atom ( $e/a$ ).<sup>[8–10]</sup> Certain investigations indicate that the rise in MT temperatures is primarily attributable to the smaller atomic radius of Ge, which results in a crystal lattice contraction and modified Mn–Mn interactions.<sup>[8,11]</sup> Nevertheless, the divergent trends observed between bulk and ribbon samples suggest that additional factors, such as grain size, enhanced chemical homogeneity, and internal stress induced by rapid solidification, also exert a significant influence.<sup>[9]</sup> These complexities underscore the necessity for a thorough structural and chemical analysis of the impact of Ge substitution on phase stability and transformation kinetics. The existing research has primarily focused on bulk materials, but there has been limited studies addressing the specific behavior of melt-spun ribbons, where rapid solidification and microstructural features could significantly affect the materials properties.

Considering the limiting research on thin ribbons and considering that one of the factors that can increase the efficiency of magnetocaloric cooling is the use of magnetocaloric materials in a low-dimensional form, in this work, we created thin ribbons of Heusler-type magnetocaloric NiCoMnSn alloys and investigated their magnetic and magnetocaloric properties as a function of Ge doping. In this study, we focused on melt-spun Ni<sub>42</sub>Co<sub>8</sub>Mn<sub>39</sub>Sn<sub>11-x</sub>Ge<sub>x</sub> ( $x = 1, 2, 3$ ) ribbons. These ribbons have inherent advantages over their bulk counterparts due to their finer grain structure, improved crystallographic texture, and high surface-to-volume ratio. These characteristics make them particularly suitable for use in active magnetic regenerator (AMR) systems.<sup>[12,13]</sup> Structural studies helped to clarify the reasons for minimization of MT hysteresis (see, e.g.,<sup>[14–16]</sup>). While most prior works on ribbon materials have relied on indirect caloric measurements, such as field-induced isothermal entropy change ( $\Delta S_{iso}$ ) derived from magnetization data, this study also incorporates direct measurements of the adiabatic temperature change ( $\Delta T_{ad}$ ), offering a more accurate assessment of the cooling capacity. Through a systematic examination of the impact of Ge substitution, our goal was to determine the optimal composition that strikes a balance between significant entropy variation, diminished MT hysteresis, and pronounced transformation properties. The findings of the present work not only deepen our comprehension of the magnetostructural transformations in MSMAs, but they also showcase the potential practicality of MSMA thin ribbons for compact solid-state refrigeration systems.

## 2. Material Synthesis and Characterization Techniques

Polycrystalline ingots of Ni<sub>42</sub>Co<sub>8</sub>Mn<sub>39</sub>Sn<sub>11-x</sub>Ge<sub>x</sub> ( $x = 1, 2, 3$ ) were synthesized by induction melting of high-purity elemental metals (>99.9%) in an argon atmosphere. For simplicity, the samples with  $x = 1, 2$ , and 3 are hereafter referred to as SnGe1, SnGe2, and SnGe3, respectively. To ensure chemical homogeneity, the ingots were re-melted several times. An excess of 3 wt.% Mn was added to the alloy to compensate for Mn losses due to evaporation during melting. Rapid solidification into ribbon form was achieved by melt-spinning at a wheel surface velocity of 30 m s<sup>-1</sup> under an Ar pressure of 10 psi using a quartz nozzle with a diameter

of 0.6 mm. The resulting ribbons were  $\approx 1$ –1.5 mm in width and 20  $\mu$ m in thickness. The ribbons were sealed in evacuated quartz tubes, heat-treated at 1173 K for 1 h, and quenched into ice water.

Microstructural analysis and compositional verification were carried out using a Hitachi TM3000 scanning electron microscope (SEM) equipped with an energy-dispersive X-ray spectroscopy (EDX) detector. Differential scanning calorimetry (DSC) was conducted using a Mettler Toledo system to determine the transformation temperatures.

Phase identification and structural evolution across MT were studied by temperature-dependent X-ray diffraction (XRD) using a Bruker D8 diffractometer (30 kV and 20 mA,  $\lambda_{Cu} = 1.5418$  Å) over the range of 194–524 K, with a step size of 10 K. To enable these measurements, the ribbons were manually ground into a fine powder. The initial X-ray diffraction data for each sample were obtained at 524 K to determine the characteristics of the high-temperature austenitic phase. Then, the samples were gradually cooled and measured at each stage.

X-ray Photoelectron Spectroscopy (XPS) measurements were carried out on a PHI QUANTERA II spectrometer with a monochromatic Al K $\alpha$  X-ray source ( $h\nu = 1486.6$  eV), operated at 15 kV with a 45° take-off angle. These measurements were used to determine the elemental composition, chemical state, and electronic state of atoms within thin layer of a material's surface.

Magnetic characterization was performed using a Quantum Design MPMS SQUID magnetometer. Magnetization measurements as a function of temperature and magnetic field were conducted to evaluate the magnetic field induced entropy change which is important characteristics of the magnetocaloric response of ribbons. For the determination of the Curie temperature of the austenite phase ( $T_C^A$ ), magnetization versus temperature measurements were performed using a home-made VSM system in the temperature range from room temperature to 450 K.

The magnetic field induced adiabatic temperature change ( $\Delta T_{ad}$ ) was directly measured under a magnetic field change of 1.96 T using a custom-built setup.<sup>[17]</sup> To eliminate thermal hysteresis artifacts, a discontinuous heating protocol was employed, in which samples were first cooled to a well-defined base temperature and then heated to the target temperature prior to each measurement. Due to the low thermal mass of individual ribbons, multiple ribbon pieces were bonded into a compact stack, with a type-K thermocouple sandwiched between them for accurate temperature measurement.

## 3. Results and Discussion

### 3.1. Crystal Structure, Microstructural, and Thermal Characterization

The crystal structure and phase evolution of the SnGe1, SnGe2, and SnGe3 melt-spun ribbons were systematically investigated using temperature-dependent XRD. The structural changes during and after the martensitic transformation can be seen in Figure S1 (Supporting Information). As shown in Figure S1 (Supporting Information), peaks associated with the martensitic phase(s) were observed to persist to relatively high temperatures (marked by arrow), indicating either a broad transformation range or the coexistence of the metastable martensitic phase

**Table 1.** Lattice parameters and  $\chi^2$  values, obtained from Rietveld refinement, and evaluated transformation volume changes ( $\Delta V/V$ ) for the studied ribbons.

Actual composition	Legend	Phase	Space Group	Lattice parameters			$\chi^2$	$\Delta V/V$ [%]
				a(Å)	b(Å)	c(Å)		
Ni <sub>41.6</sub> Co <sub>8</sub> Mn <sub>39.8</sub> Sn <sub>9.6</sub> Ge <sub>1.1</sub>	SnGe1	Cubic (524 K)	Fm-3m	5.950 ± 0.001	–	–	1.07	0.56
		NM Tetragonal (194K)	P4/mmm	3.918 ± 0.001	3.919 ± 0.001	6.728 ± 0.004	1.05	
		7 M	C2/m	4.389 ± 0.001	5.276 ± 0.002	21.052 ± 0.006		
Ni <sub>41.4</sub> Co <sub>8.2</sub> Mn <sub>39.4</sub> Sn <sub>8.8</sub> Ge <sub>2.2</sub>	SnGe2	Cubic (524 K)	Fm-3m	5.947 ± 0.001	–	–	1.20	0.48
		NM Tetragonal (234K)	P4/mmm	3.919 ± 0.002	3.919 ± 0.002	6.730 ± 0.006	1.21	
		7 M	C2/m	4.394 ± 0.001	5.409 ± 0.006	21.036 ± 0.005		
Ni <sub>41.8</sub> Co <sub>7.7</sub> Mn <sub>39.5</sub> Sn <sub>7.8</sub> Ge <sub>3.2</sub>	SnGe3	Cubic (524 K)	Fm-3m	5.926 ± 0.001	–	–	1.02	0.51
		NM Tetragonal (194K)	P4/mmm	3.911 ± 0.001	3.911 ± 0.001	6.690 ± 0.003	1.13	
		7 M	C2/m	4.367 ± 0.001	5.299 ± 0.002	20.935 ± 0.004		

and the austenitic phase over an extended temperature interval. This broadening may be due, in part, to the influence of internal stresses, particularly those introduced during sample preparation, such as ribbon grinding. Additionally, limited thermal contact between the powder and the XRD stage may contribute by creating local temperature gradients.

Structural analysis was performed using the Le Bail refinement with the FullProf software. As a representative case, Rietveld-refined XRD patterns for SnGe2 are presented at selected temperatures, corresponding to the nearly complete austenitic phase, an intermediate transformation state, and a predominantly martensitic phase (Figure 1). As summarized in Table 1, at high temperatures (e.g., 524 K), all compositions exhibited a cubic austenitic structure with space group *Fm-3m*, which is characteristic of the parent austenite phase. The refined lattice parameters *a* for the cubic austenitic phase were determined to be 5.950 ± 0.001 Å (SnGe1), 5.947 ± 0.001 Å (SnGe2), and 5.925 ± 0.001 Å (SnGe3), indicating a systematic decrease with increasing Ge content.<sup>[4]</sup>

At lower temperatures, the martensitic structure becomes complex, consisting of a mixture of phases. Both non-modulated and modulated martensitic structures were observed, indicating a structural heterogeneity in the low-temperature region. The dominant martensitic phase was identified as an L1<sub>0</sub>-type tetragonal structure with space group *P4/mmm*, commonly found in Ni-Mn-based Heusler alloys.<sup>[13,18,19]</sup> Additional diffraction peaks were ascribed to a 7 M modulated monoclinic structure with the space group *C2/m*. The formation of modulated martensitic structures, such as 5, 7, 10, and 14 M, is typical for Ni-Mn-X (X = Ga, Sn, In) Heusler alloys, which is affected by both composition and processing methods.<sup>[20,21]</sup> These modulations are believed to occur in order to reduce the energy at the interface between the austenitic and martensitic phases.

A crucial parameter associated with the first-order martensitic transformation is the relative change in unit cell volume ( $\Delta V/V = (V_A - V_M)/V_M$ ), where  $V_A$  and  $V_M$  are the unit cell volumes of the austenitic and martensitic phases, respectively. Accurately determining  $\Delta V/V$  across the transformation region from XRD data can be challenging due to the presence of latent heat effects and temperature instabilities associated with the first-order phase transition. To address this issue, an extrapolation method

has been employed to estimate  $\Delta V/V$  values across the transformation (see Figure 2a).<sup>[14]</sup> The calculated percentage variations in volume for each composition are presented in Table 1. Table 1 demonstrates that the SnGe2 ribbon exhibits the smallest transformation-induced volume change among the tested ribbons. A reduced  $\Delta V/V$  ratio is generally considered as an indication of improved geometric compatibility between the austenitic and martensitic crystal lattices.<sup>[16]</sup> Such compatibility is crucial for the reversibility of the transformation and typically leads to lower internal stresses, reduced transformation hysteresis, and a narrower transformation front.<sup>[16,22]</sup>

### 3.1.1. Transformation Characteristics

Figure 2b presents the DSC cooling and heating curves for all melt-spun ribbons. Each sample exhibits a distinct endothermic peak, corresponding to the martensite-to-austenite transformation. With increasing Ge content, the reverse transformation start ( $A_s$ ) and finish ( $A_f$ ) temperatures shift to higher values. Specifically, an initial increase of  $\approx 17$  K is observed from SnGe1 to SnGe2, whereas from SnGe2 to SnGe3 the peak transformation temperature shifts slightly (by about 4 K) toward lower value. Since Sn and Ge have the same number of valence electrons, the electron concentration ( $e/a$ ) remains unchanged with Ge doping. Therefore, the observed shift in transformation temperatures cannot be attributed to variations in  $e/a$ . Instead, it is more likely linked to the smaller atomic radius of Ge compared to Sn, which leads to a reduction in the lattice parameter (see Table 1), modifies Mn–Mn interatomic distances, and alters the magnetostructural coupling. Herein, the transformation entropy change ( $\Delta S_{tr}$ ) was estimated from DSC heating data. The enthalpy change ( $\Delta H$ ) was obtained by integrating the area under the endothermic peak of the DSC curve, and  $\Delta S_{tr}$  was then calculated as  $\Delta H$  divided by the average transformation temperature, defined as  $(A_s + A_f)/2$ . The resulting  $\Delta S_{tr}$  values are summarized in Table 2. The inset of Figure 2 b shows the surface morphology of SnGe2 sample at 250 K. According to the DSC results, the sample is in the martensitic phase at this temperature. The most prominent feature in the image is the well-defined twin structure within individual grains. The formation of the twin structure is a key

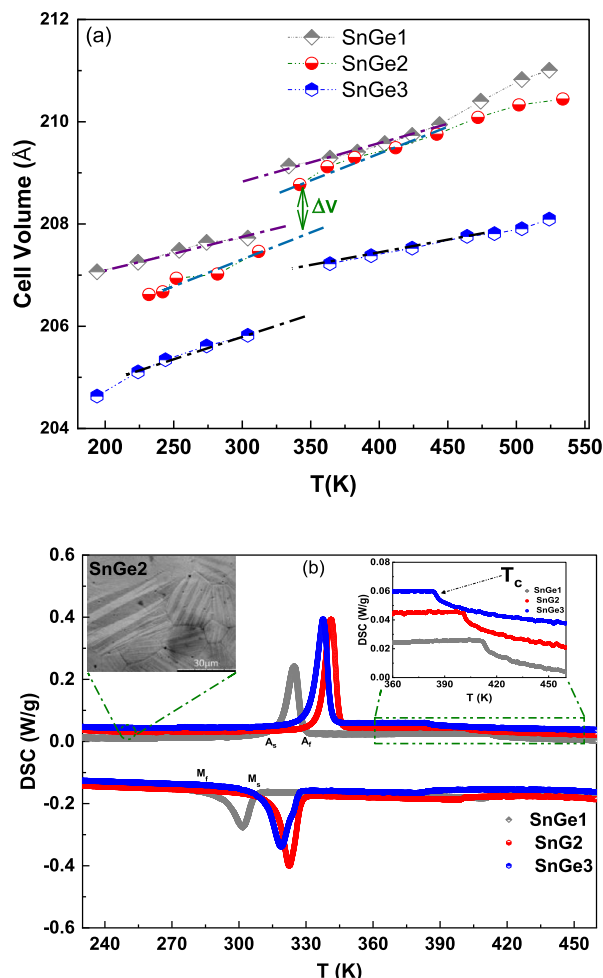


**Figure 2.** a) Unit cell volume versus temperature dependences for SnGe1, SnGe2, and SnGe3 ribbons calculated using Rietveld analysis of the X-ray data; b) DSC cooling and heating curves for all ribbons. Inset: SEM image of SnGe2 showing twin microstructure of martensitic phase and Curie temperature of austenite phase  $T_C^A$ .

mechanism for minimizing the overall strain energy associated with the martensitic transformation from the high-symmetry austenitic phase to the low-symmetry martensitic phase.

### 3.1.2. Microstructure and Chemical Homogeneity

To gain insight into the effect of grain size on the martensitic transformation temperature, SEM images were captured for all

the samples at room temperature. Microscopic analysis of the melt-spun ribbons (wheel-contacted surface) (Figure 3), reveals that increasing the Ge doping level results in a noticeable reduction in grain size. While the decrease in grain size is relatively minor in the SnGe2 sample, it becomes clearly pronounced in SnGe3. In the SnGe3 sample, the reduced grain size acts as a kinetic barrier to MT by increasing grain boundary area, which tends to suppress the MT temperature, as supported by prior studies.<sup>[23,24]</sup> This effect competes with the thermodynamic impact of a reduced unit cell volume, which typically leads to an increase in the transformation temperature. This may explain why, for SnGe3, only a small shift of about 4 K toward lower temperatures is observed compared to SnGe2, despite the reduction in unit cell volume. Furthermore, as shown in Figure 3d, the SnGe3 sample contains a significant amount of ultrafine grains smaller than 1  $\mu\text{m}$ , which may further contribute to the broadening of the transformation and its suppression.

EDS measurements with the uncertainty of 0.5 at. % were conducted to clarify the chemical composition and its uniformity across the total ribbon area. Five spots, both on the free surface and on the wheel-contact side, of each ribbon were analyzed. The averaged measured compositions for SnGe1, SnGe2, and SnGe3 are presented in Table 1. These values closely match the nominal compositions of  $\text{Ni}_{42}\text{Co}_8\text{Mn}_{39}\text{Sn}_{10}\text{Ge}_1$ ,  $\text{Ni}_{42}\text{Co}_8\text{Mn}_{39}\text{Sn}_9\text{Ge}_2$ , and  $\text{Ni}_{42}\text{Co}_8\text{Mn}_{39}\text{Sn}_8\text{Ge}_3$ , respectively, indicating precise control over elemental ratios during synthesis. In addition, the good agreement between the free and wheel-contact surfaces suggests a uniform elemental distribution across the ribbon thickness.

SEM images of the ribbon surfaces are shown in Figure 3. They demonstrate a significant result: the grain size decreases from  $\approx 20 \mu\text{m}$  in SnGe1 to about  $10 \mu\text{m}$  in SnGe3 sample as a function of Ge doping. This pronounced grain refinement with higher Ge doping is attributed to the influence of Ge on the solidification dynamics, leading to the formation of finer grains. Each crystallographic grain exhibits a well-oriented martensitic microstructure. However, the grain structure as a whole does not show a crystallographic texture on the ribbon surface. In Figure 3c,d one can see precipitates at the grain boundaries of the SnGe3 ribbon.

The XPS analysis was used to obtain more evidence of the high chemical homogeneity of the ribbons under study. XPS method examines the atomic electronic configurations and element spatial distribution in the material. Figure 4a shows the wide-scan survey spectrum, where the core-level signals of Ni, Co, Mn, Sn, and Ge can be clearly identified. To gain insight into the valence states and possible surface oxidation, we conducted high-resolution core-level scanning. The core-level spectra of Ni, Mn, and Co exhibit binding energies characteristic of their metallic states, with peaks centered at 852.7 (870.0) eV, 641.2(653.0) eV,

**Table 2.** Values of the martensitic characteristic temperatures and austenite Curie temperature ( $T_C^A$ ), the MT hysteresis width ( $\Delta T_{\text{hys}}$ ) defined as the difference between the peak positions of the first derivative of cooling and heating branches of the  $M(T)$  curve measured at a magnetic field of 0.1 T;  $\Delta S_{\text{iso}}$  (from the Maxwell relation) and  $\Delta S_t$  (from the Clausius–Clapeyron equation) at 7 T; and  $\Delta S_{\text{tr}}$  (from DSC).

Ribbons	$M_s$ [K]	$M_f$ [K]	$A_s$ [K]	$A_f$ [K]	$T_C^A$ [K]	$\Delta T_{\text{hys}}$ [K]	$\Delta S_{\text{iso}}$ [J/kgK] Maxwell	$\Delta S_t$ [J/kgK] C-C	$\Delta S_{\text{tr}}$ [J/kgK] DSC
SnGe1	308.2	300.8	323.2	327.4	421.9	20.5	26.2	21.1	26.9
SnGe2	331.4	323.6	339.3	343.3	411.5	12.1	35.5	32.9	38.5
SnGe3	325.5	319.5	337.1	341.7	391.1	16.1	27.1	30.1	37.2

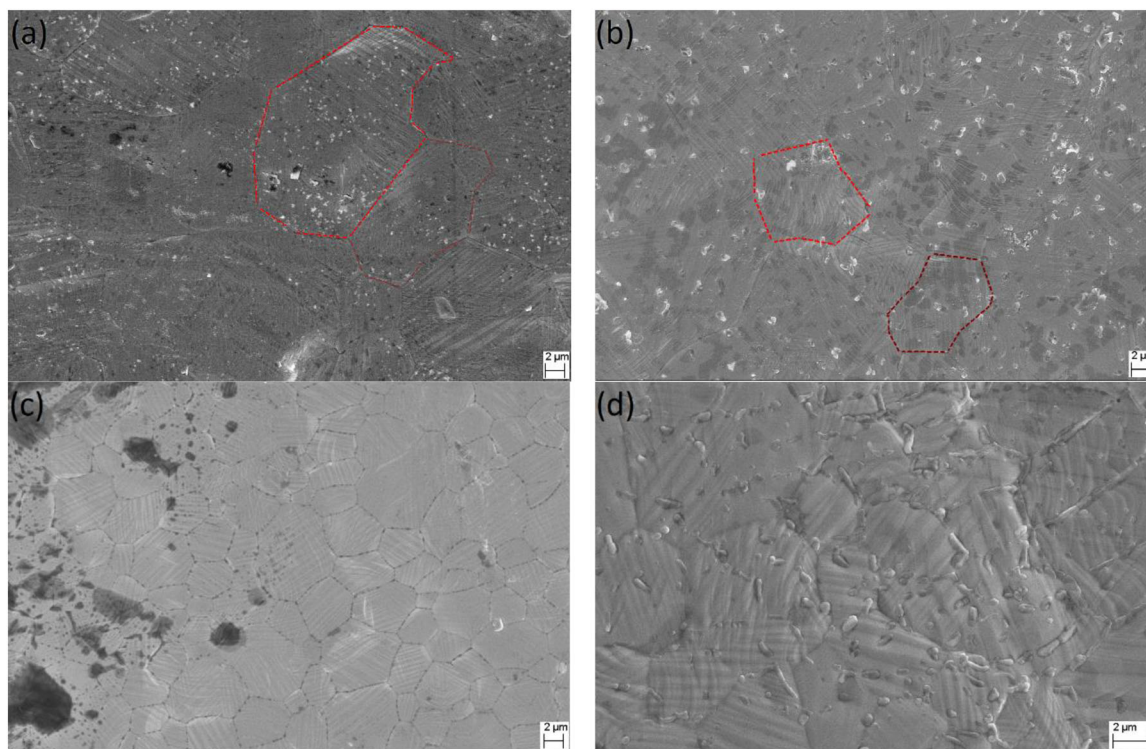


**Figure 3.** SEM images of  $\text{Ni}_{42}\text{Co}_8\text{Mn}_{39}\text{Sn}_{11-x}\text{Ge}_x$  ribbons: a–c) wheel-side surfaces of SnGe1, SnGe2, and SnGe3 ribbons, respectively, showing progressive grain refinement with increasing Ge content; d) grain size distribution on the free surface of SnGe3. Dashed lines in (a) and (b) have been added to make the grain boundaries more easily visible.

and 780.7(796.5) eV for  $\text{Ni}2p_{3/2}$  ( $\text{Ni}2p_{1/2}$ ),  $\text{Mn}2p_{3/2}$  ( $\text{Mn}2p_{1/2}$ ) and  $\text{Co}2p_{3/2}$  ( $\text{Co}2p_{1/2}$ ), respectively.<sup>[25]</sup> For Ni, a shoulder at  $\approx 855$  eV and satellite features between 861 and 873 eV are observed, indicating minor surface oxidation.<sup>[26]</sup> The core-level spectra for Sn and Ge are presented in Figure 4e,g. Metallic  $\text{Sn}^0$  is identified by the peaks at  $\approx 24.0$  eV ( $\text{Sn}4d_{5/2}$ ), 486.3 eV ( $\text{Sn}3d_{5/2}$ ) and 494.5 eV ( $\text{Sn}3d_{3/2}$ ), while metallic  $\text{Ge}^0$  appears at 29.4 eV (Ge 3d). In addition, oxidized components are detected at 25.2 eV ( $\text{Sn}^{4+}4d_{5/2}$ ), 495.6 eV ( $\text{Sn}^{4+}3d_{5/2}$ ), and  $\approx 31.7$  eV ( $\text{Ge}^{4+}3d$ ). The simultaneous presence of the metallic peaks strongly indicates that Sn and Ge maintain their metallic states within the bulk of the material, whereas oxidized components are considered as located on the ribbons surface. To resolve potential peak overlap between Ge 3d and Sn 4d, a separate high-resolution scan of the Ge  $2p_{3/2}$  orbital was carried out (inset of Figure 4e). A distinct peak at  $\approx 1219.4$  eV was observed, and it was found to increase progressively as the Ge doping increased, confirming the effective incorporation of Ge into the volume of alloy matrix. This outcome is further supported by a semi-quantitative analysis based on the integrated areas of Ge 2p and Sn 3d peaks, corrected using relative sensitivity factors (RSF). The results demonstrate a clear increasing trend in Ge content across the series, as expected. Together with the EDS findings, these XPS results provide strong evidence of Ge effective incorporation into the alloy matrix. To further substantiate this interpretation, Figure S2 (Supporting Information) presents a detailed peak deconvolution of the elemental spectrum for a representative sample of SnGe2.

### 3.2. Magnetic Properties

**Figure 5** displays the isofield magnetization as a function of temperature,  $M(T)$ , for the studied ribbons, measured under applied magnetic fields ranging from 0.1 T to 7 T using both field-cooling (FC) and field-heating (FH) protocols. These data indicate the presence of distinct phase changes. Upon cooling from the paramagnetic austenitic state, the magnetization typically increases as the samples pass through the Curie temperature of the austenite phase ( $T_C^A$ ), indicating a transition to a ferromagnetic austenite. This is followed by a sharp decrease in magnetization at the forward MT in the FC protocol, corresponding to the formation of the magnetically weaker martensite phase. During subsequent heating, the reverse MT occurs, marked by an increase in magnetization as the martensite reverts to the ferromagnetic austenite, followed by a decrease as the temperature exceeds  $T_C^A$ , and the austenite becomes paramagnetic once again. A distinct thermal hysteresis ( $\Delta T_{\text{hys}}$ ) between the heating and cooling  $M(T)$  curves is evident for all samples, which is the characteristic of a first-order phase transition (FOPT).<sup>[27,28]</sup> The characteristic MT temperatures, martensitic start ( $M_s$ ) and finish ( $M_f$ ), austenitic start ( $A_s$ ) and finish ( $A_f$ ), were determined using the two-tangent method applied to  $M(T)$  curve measured at a 0.1 T magnetic field. They are summarized in Table 2. The austenitic Curie temperature,  $T_C^A$ , was determined from the extremum in the first derivative of the  $M(T)$  curves measured using a different instrument, as the current machine is limited to 400 K.

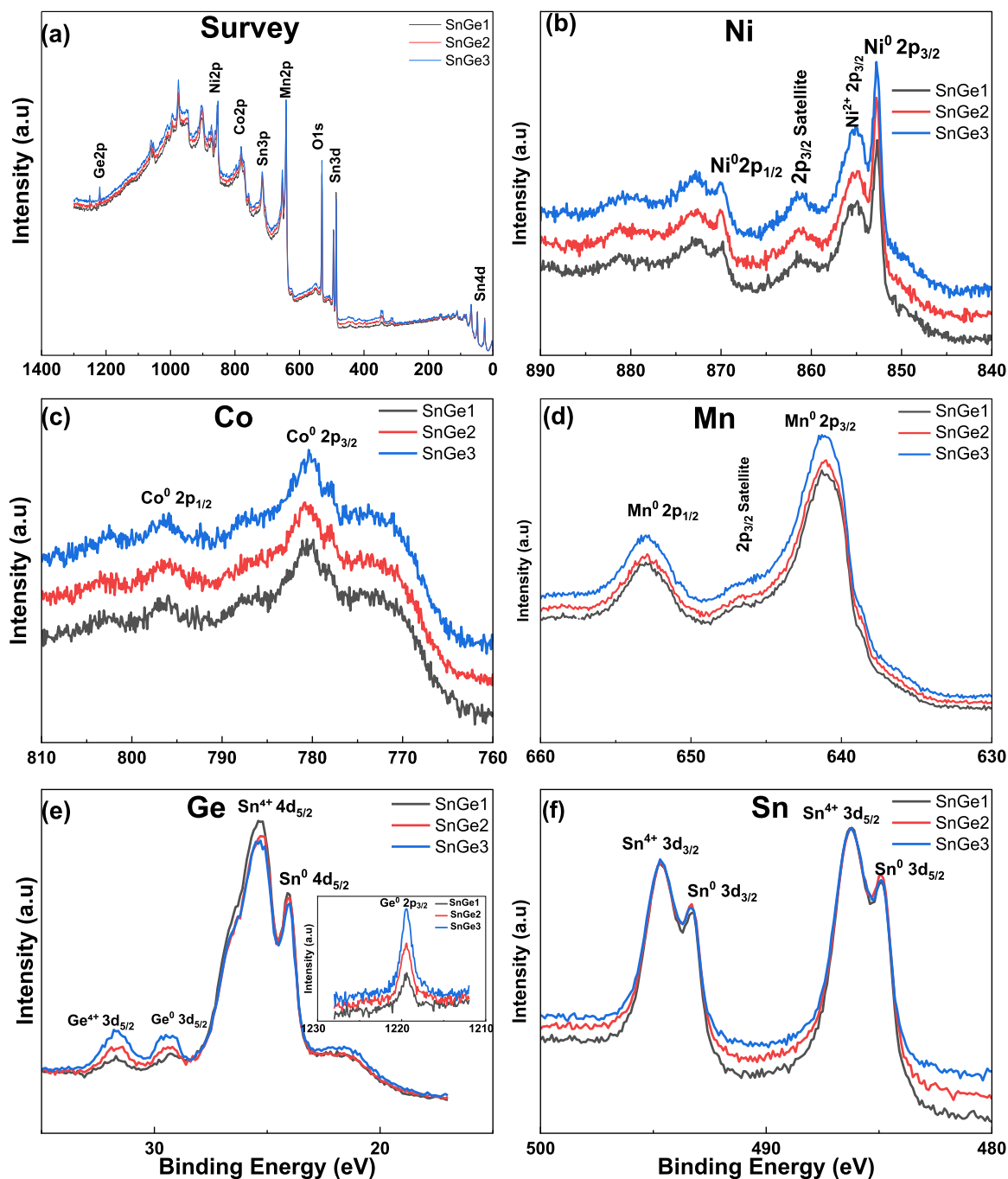


**Figure 4.** Survey and high-resolution XPS spectra of SnGe1, SnGe2, and SnGe3 alloys. a) Survey spectrum confirming the presence of Ni, Co, Mn, Sn, and Ge. Panels b–f) show core-level spectra of Ni, Co, Mn, Ge, and Sn, with features corresponding to metallic and oxidized states, as well as satellite structures where applicable.

Figure 5 shows that with the increase of the magnetic field, MT anomaly shifts to lower temperatures meaning that the magnetic field energetically stabilizes the austenitic phase, which possesses a higher magnetization compared to the martensitic phase. As a result, the austenite phase becomes thermodynamically favorable at lower temperatures under an applied field. Consequently, less thermal energy is required to induce the reverse transformation (martensite to austenite),

or further cooling is necessary to trigger the forward transformation (austenite to martensite).<sup>[2,28]</sup> Each of the insets in Figure 5 shows the linear fit of the magnetic field dependence of the MT temperature, derived from the heating curves, specifically, the austenite start temperature  $A_s$ . The MT temperature shifts linearly to its lower values with the slope,  $\frac{dT_{As}}{\mu_0 dH}$ , equal to -4.8, -2.8 and -2.2 K/T for SnGe1, SnGe2 and SnGe3, respectively.

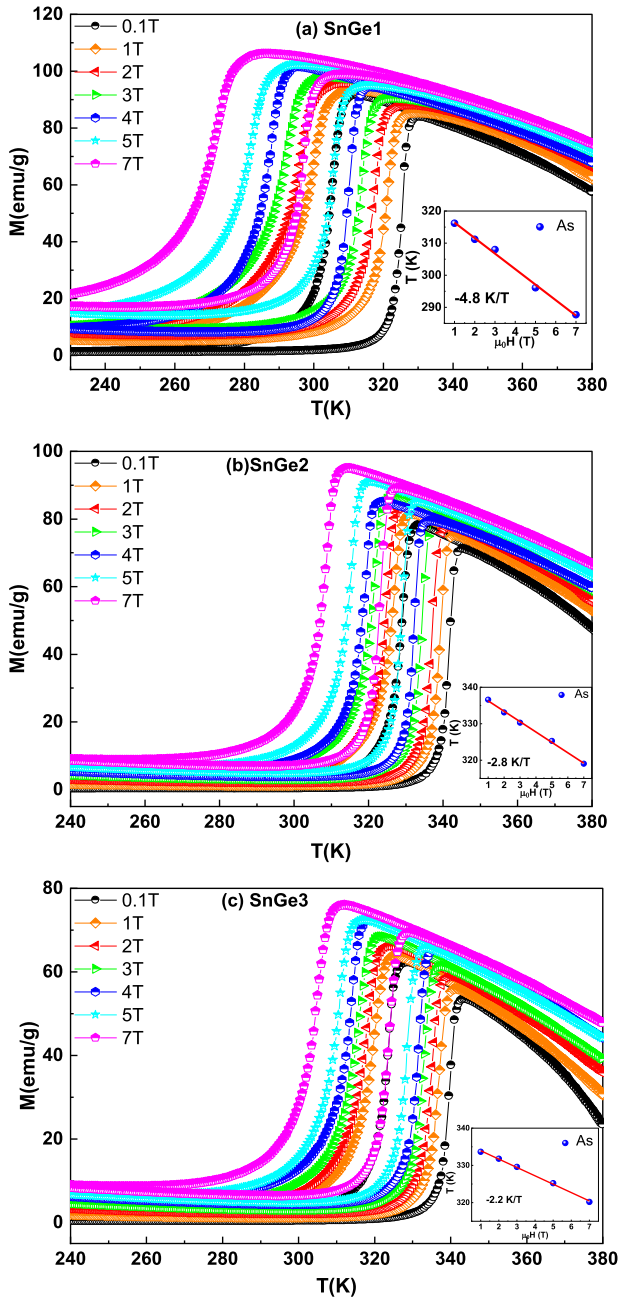


**Figure 5.** Thermomagnetization curves for the  $\text{Ni}_{42}\text{Co}_8\text{Mn}_{39}\text{Sn}_{1-x}\text{Ge}_x$  ( $x = 1$  a), 2 b), and 3 c)) ribbons measured under different applied magnetic fields up to 7 T. The inset of each figure depicts the  $A_3$  versus magnetic field dependences and corresponding slopes of linear approximations in K/T.

The associated with MT change in magnetization ( $\Delta M$ ) significantly varies with the Ge content. Here,  $\Delta M$  is defined as the difference in magnetization values near the  $A_3$  and  $A_f$  temperatures under an applied magnetic field of 0.1 T. The values of  $\Delta M$  were determined to be 80, 69, and 51  $\text{Am}^2/\text{kg}$  for SnGe1, SnGe2, and SnGe3, respectively. A substantial  $\Delta M$  is crucial for a pronounced magnetocaloric effect (MCE), as it indicates a strong magneto-structural coupling and enables a significant field-induced shift

of the MT temperature.<sup>[27,28]</sup> However, in inverse magnetocaloric MSMA, the role of  $\Delta M$  possesses a well-known challenge, often referred to as a “dilemma”.<sup>[1,27,28]</sup> On the one hand, a large  $\Delta M$  facilitates the magnetocaloric effect, on the other hand, a large  $\Delta M$  increases the magnetic entropy change ( $\Delta S_m$ ), which opposes the lattice entropy change ( $\Delta S_{lat}$ ), potentially offsetting the total entropy gain,  $\Delta S_t = \Delta S_{lat} + \Delta S_m$ .<sup>[1,2,28]</sup> Therefore, it is desirable to find the optimal value of  $\Delta M$  in order to maximize the useful MCE.

The width of transformation front, which is defined as  $A_f - A_s$ , varies depending on the Sn/Ge ratio and ranges from 4 to 7 K for all the samples (Figure 5). The SnGe2 sample exhibits the sharpest transformation with a width of 4 K. The broadening of MT is often attributed to chemical inhomogeneity and variations in the atomic order, which can lead to a distribution of MT temperatures within the material.<sup>[27,29]</sup> In our case, the narrow transformation front is thought to be the result of both significant chemical homogeneity (see Section 3.1.3) and good  $L2_1$ -atomic order (e.g., see peaks at  $2\theta \approx 25^\circ$  and  $31^\circ$  in Figure 1) in the ribbons.<sup>[29]</sup>

The width of the MT thermal hysteresis ( $\Delta T_{hys}$ ), defined as the difference between the peak positions of the first derivative of cooling and heating branches of the  $M(T)$  curves measured at a magnetic field of 0.1 T in Figure 5, is 20.5 K, 12.1 K and 16.1 K for SnGe1, SnGe2 and SnGe3, respectively. The lower  $\Delta T_{hys}$  value in the SnGe2 ribbon suggests better crystallographic compatibility between martensitic and austenitic phases, which is a key factor in minimizing hysteresis, as discussed by Pfeuffer et al.<sup>[2]</sup> Generally, hysteresis arises from both intrinsic factors, such as magnetic interactions, the electronic structure, and the fundamental nature of the first-order phase transition (FOPT), and extrinsic factors, such as microstructure, lattice defects, internal stresses, grain boundaries, and compositional uniformity. The finding that SnGe1, with the lowest MT temperature, exhibits the largest  $\Delta T_{hys}$  is in line with reports for certain Heusler-type MSMA, where hysteresis tended to increase at lower transition temperatures.<sup>[28]</sup> This can be explained by the disparity in the shift of the forward and reverse transformation branches, which is caused by the varying temperature dependence of the underlying thermodynamic forces, including magnetic effects. Microstructural features, such as grain size, defect density, and internal stresses, which can be altered by processing and heat treatment, also significantly contribute to  $\Delta T_{hys}$ .<sup>[27,29,30]</sup> A slight increase in  $\Delta T_{hys}$  with applied magnetic field was also noted, which is consistent with a more pronounced field-induced shift of the forward MT (on cooling) compared to the reverse MT (on heating), often linked to the increasing amount of the low temperature FM contribution.<sup>[31,32]</sup>

The MT temperature has an increasing trend with rising Ge/Sn ratio. Changes in atomic volume and interatomic distances are likely responsible for this, as they result from the different atomic radii of Sn and Ge. The substitution of larger Sn atoms with smaller Ge atoms leads to a contraction of the unit cell volume. This lattice shrinkage modifies interatomic distances, particularly the Mn-Mn spacing, which is critical for magnetic exchange interactions. Furthermore, a reduced unit cell volume can enhance the hybridization between Ni 3d and Mn 3d electronic states.<sup>[33]</sup> Such modifications in electronic structure and bonding between atoms can stabilize the martensitic phase, thereby

shifting MT to higher temperatures. The less pronounced increase in the MT temperature for the SnGe3 sample, despite the expected further reduction in unit cell volume, suggests that other factors might be influencing the process. While atomic size effects should be prominent, here a lower degree of atomic order in the SnGe3 sample could counteract the effect of volume change.<sup>[34]</sup> Thus, various factors, such as the precise degree of atomic order, the specific site occupancy of constituent atoms, the details of electronic hybridization, and microstructural features such as grain size, chemical segregation, and internal stress, all influenced by the melt spinning process, collectively determine the MT behavior.<sup>[9,30,34,35]</sup>

The Curie temperature of the austenite phase ( $T_C^A$ ) decreases with increasing Ge content, reducing from  $\approx 421.9$  K in SnGe1 to 411.5 K in SnGe2 and 391.9 K in SnGe3. This trend indicates a weakening of net ferromagnetic exchange interactions within the austenite phase, likely due to the shrinkage of the unit cell volume and the resulting modification of key interatomic distances (such as Mn–Mn and Mn–Co) that govern magnetic coupling.<sup>[8]</sup> Even though previous studies suggest that  $T_C^A$  is primarily affected by the nature of interactions at the Ni and Mn sites and is relatively insensitive to Sn content, it is important to note that atomic disorder, shaped by processing conditions such as heat treatment, can also influence the Curie temperature.<sup>[34]</sup> Moreover, even minor variations in the actual Co content can cause noticeable shifts in the Curie temperature.<sup>[1]</sup> For instance, Ito et al.<sup>[36]</sup> reported a shift of about 54 K in the Curie temperature upon substituting 2.5 at.% Co for Ni. Since the magnetization in Ni–Co–Mn–Sn Heusler alloys mainly arises from Mn and Co atoms, the magnetic ordering temperatures are highly sensitive to both Mn–Mn and Mn–Co interatomic distances.<sup>[35]</sup> Thus, a decline in  $T_C^A$  upon Ge substitution might also result from subtle changes in Co–Mn spacing, potentially enhancing antiferromagnetic interactions or altering the overall balance of magnetic exchange within the crystal lattice.

### 3.3. Magnetocaloric Effect

The magnetic field induced isothermal entropy change ( $\Delta S_{iso}$ ) can be calculated from the experimental thermomagnetic curves,  $M(T)$ , measured under isofield conditions using a numerical approximation of the Maxwell relationship (see, e.g.<sup>[37,38]</sup>):

$$\Delta S_{iso}(T_j, \Delta H) = \sum_{i=1}^{n-1} \frac{1}{2} \left[ \left( \frac{\partial M_i}{\partial T_j} \right)_{H_i} + \left( \frac{\partial M_{i+1}}{\partial T_j} \right)_{H_{i+1}} \right] \Delta H \quad (1)$$

where  $\left( \frac{\partial M_i}{\partial T_j} \right)_{H_i}$  is the first derivative of magnetization at applied magnetic field of  $H_i$  and  $\Delta H$  is the magnetic field step used in different measurements of thermomagnetization curves. The 3D charts depicting the dependence of  $\Delta S_{iso}$  as a function of temperature and a field changes up to 7 T, are presented in **Figure 6**. The maximums of  $\Delta S_{iso}$  for the SnGe1, SnGe2 and SnGe3 ribbons under a magnetic field change of 7 T are equal to 26.2, 35.5, and 27.1 J kg<sup>-1</sup> K<sup>-1</sup>, respectively (Table 2). For all compositions, a positive  $\Delta S_{iso}$  peak is observed, indicating that the entropy of the system increases when a magnetic field is applied isothermally. This behavior is typical for materials undergoing a field-induced re-

verse martensitic transformation from a low-magnetization (typically weak magnetic or antiferromagnetic martensite) to a high-magnetization (ferromagnetic austenite) phase. As mentioned before, contributions of lattice and magnetic entropy have opposite signs; for an inverse MCE observed during the martensite-to-austenite transformation,  $\Delta S_{lat}$  is typically positive, while  $\Delta S_{mag}$  (associated with the change from a weakly magnetic martensite to a more strongly magnetic austenite) can be negative.<sup>[39,40]</sup> During the transformation from the martensitic to the austenitic phase, the positive contribution from  $\Delta S_{lat}$  is often predominant, leading to an overall positive peak characteristic of the inverse MCE. A more profound analysis of the entropy variations, particularly in the case of the SnGe2 sample, which demonstrates a substantial  $\Delta S_{iso}$ , can be achieved by examining the interdependence of various factors. The well-known Clausius–Clapeyron (C–C) equation for a first-order phase transition, adapted for magnetic systems, is usually expressed as:

$$\Delta S_t = - \frac{\Delta M}{dT/d(\mu_0 H)} \quad (2)$$

Here,  $\Delta S_t$  represents the total transformation entropy,  $\Delta M$  is the difference in magnetization between the austenite and martensite phases, and  $dT/d(\mu_0 H)$  is the shift of the MT temperature caused by the applied magnetic field. Both  $\Delta M$  and  $dT/d(\mu_0 H)$  are critical parameters influencing the achievable  $\Delta S_t$ . A larger field-induced shift of MT implies a more significant amount of the martensitic phase converted into austenite under a given magnetic field, which is advantageous for maximizing the extrinsic structural contribution,  $\Delta S_{lat}(f)$ , where  $f$  is the volume fraction of the martensitic phase transformed, to the total entropy change. However, a larger  $dT/d(\mu_0 H)$  is often associated with materials that also exhibit a substantial  $\Delta M$ . While a large  $\Delta M$  is generally favorable for a strong magnetocaloric response, it also signifies a considerable difference in the magnetic order between the two phases, which in turn affects the  $\Delta S_{mag}$  contribution to the total entropy change. This creates a scenario where optimizing these parameters is crucial, as an excessively large contribution from one might not always translate to the maximum net  $\Delta S_t$ . An optimal balance between the magnitude of the field-induced shift of MT and the change in magnetization at MT seems to be necessary to achieve a high total isothermal entropy change, as observed in the SnGe2 sample. The entropy change obtained from the Clausius–Clapeyron approach ( $\Delta S_t$ ) was calculated and is reported in Table 2. The values are comparable to those derived from the Maxwell relation and from DSC, confirming that the Maxwell-based  $\Delta S_{iso}$  values are reliable in the present work and do not exhibit the artificial spikes around the transition temperature.

For magnetocaloric applications, it is crucial to obtain a sufficiently large MCE under magnetic fields that are not exceeding 2 T, achievable with permanent magnets. **Figure 7** shows a comparison of the  $\Delta S_{iso}$  values for a range of Ni–Mn-based Heusler alloys, both in bulk and ribbon form, along with our fabricated ribbons, measured under a 2 T magnetic field change, to highlight the difference in magnetocaloric response between bulk and ribbon samples. Remarkably, the SnGe2 ribbon exhibits the highest  $\Delta S_{iso}$  among the series, reaching about 22.8 J kg<sup>-1</sup> K<sup>-1</sup>.

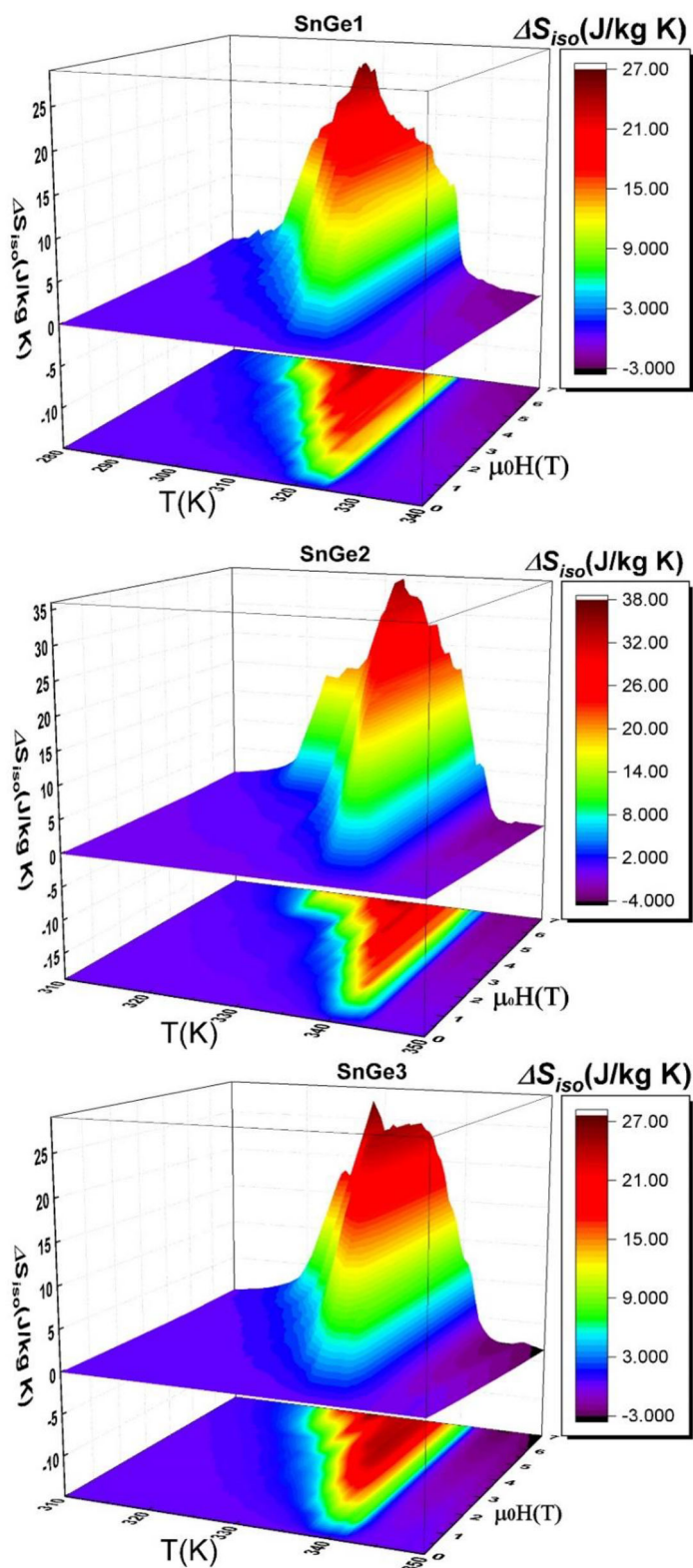


**Figure 6.** Three-dimensional contour charts of the entropy change ( $\Delta S_{iso}$ ) as a function of temperature and magnetic field for SnGe1, SnGe2, and SnGe3 ribbons.

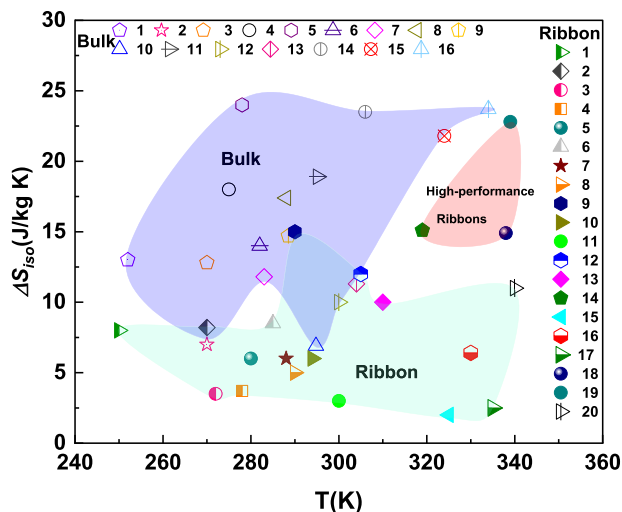


**Figure 7.** Comparison of the peak isothermal magnetic entropy change ( $|\Delta S_{150}|$ ) versus peak temperature at 2 T for the present SnGe-series melt-spun ribbons with selected bulk and ribbon reported, all belonging to the class of Ni–Mn–X (X = In, Sn) Heusler alloys. Data for bulk materials are taken from: 1,<sup>[41]</sup> 2,<sup>[42]</sup> 3,<sup>[43]</sup> 4,<sup>[44]</sup> 5,<sup>[45]</sup> 6,<sup>[1]</sup> 7,<sup>[46]</sup> 8,<sup>[47]</sup> 9,<sup>[48]</sup> 10,<sup>[49]</sup> 11,<sup>[46]</sup> 12,<sup>[50]</sup> 13,<sup>[28]</sup> 14,<sup>[28]</sup> 15,<sup>[28]</sup> 16,<sup>[28]</sup> Data for ribbon-form materials are taken from: 1,<sup>[51]</sup> 2,<sup>[52]</sup> 3,<sup>[53]</sup> 4,<sup>[14]</sup> 5,<sup>[51]</sup> 6,<sup>[54]</sup> 7,<sup>[55]</sup> 8,<sup>[51]</sup> 9,<sup>[30]</sup> 10,<sup>[53]</sup> 11,<sup>[51]</sup> 12,<sup>[4]</sup> 13,<sup>[54]</sup> 14 (this work), 15,<sup>[56]</sup> 16,<sup>[54]</sup> 17,<sup>[53]</sup> 18, and 19 (this work), 20.<sup>[57]</sup>

The experiment demonstrates that the form of the MCE material, whether it is in bulk or in the form of a melt-spun ribbon, plays a significant role in determining its functional properties. The manufacturing process has a significant impact on the composition homogeneity and microstructure, including grain size, crystallographic texture, and defect density.<sup>[37]</sup> These factors, in turn, influence the magnetostructural properties and MCE of the material. In particular, melt-spun ribbons often exhibit composition variation, finer grain sizes, a higher density of quenched-in defects, and residual stresses resulting from rapid solidification. These microstructural features can expand the MT front, resulting in a reduction of the volume fraction of the field-induced austenitic phase, thus reducing MCE.<sup>[23]</sup> Despite these potential limitations, our ribbons, especially SnGe2, demonstrate outstanding magnetocaloric performance. As illustrated in Figure 7, the  $\Delta S_{150}$  values of our ribbons not only exceed those of many previously reported Ni–Mn-based MSMA ribbons, but they also rival the same MSMA in a bulk form under similar magnetic field conditions. The outstanding MCE performance of our ribbons can be attributed, in the first place, to their exceptional chemical and structural uniformity, which was achieved through the rapid solidification of small-sized ribbons ( $\approx 1$  mm wide and  $\approx 20$   $\mu$ m thick).

Figure 8 compares the peak values of  $\Delta S_{150}$  and corresponding MT temperatures for the studied ribbons with a wide range of magnetocaloric materials reported in the literature, all measured under a 2 T magnetic field change. The SnGe2 ribbon exhibits particularly high performance, which is comparable to or even exceeds that of several other materials with first-order transitions, including Heusler-type MSMA and selected rare-earth-based compounds. The retention of a strong magnetocaloric response in the ribbons can be attributed to several factors, in-

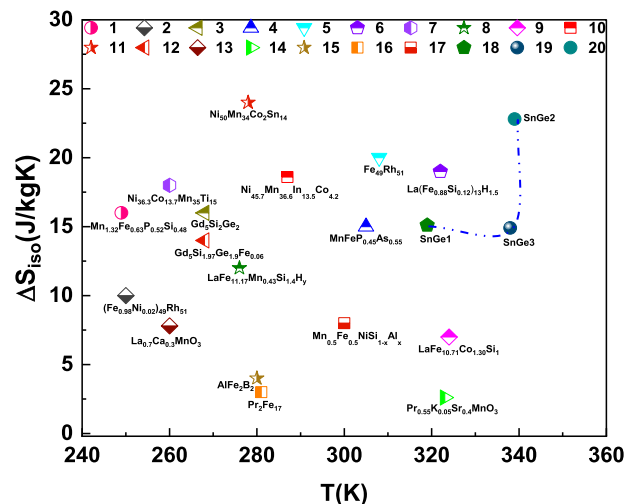


**Figure 8.** Comparison of the peak isothermal magnetic entropy change ( $|\Delta S_{150}|$ ) versus peak temperature for the Ni<sub>42</sub>Co<sub>8</sub>Mn<sub>39</sub>Sn<sub>11-x</sub>Ge<sub>x</sub> ribbons (SnGe1, SnGe2, and SnGe3) with various magnetocaloric materials in different forms (bulk and ribbons) reported in the literature, under a magnetic field change of 2 T. Data for other materials are taken from: 1,<sup>[58]</sup> 2,<sup>[31]</sup> 3,<sup>[59]</sup> 4,<sup>[60]</sup> 5,<sup>[61]</sup> 6,<sup>[62]</sup> 7,<sup>[63]</sup> 8,<sup>[27]</sup> 9,<sup>[27]</sup> 10,<sup>[28]</sup> 11,<sup>[45]</sup> 12,<sup>[64]</sup> 13,<sup>[65]</sup> 14,<sup>[1]</sup> 15,<sup>[67]</sup> 16,<sup>[68]</sup> 17,<sup>[69]</sup> 18, 19, and 20 (this work).

cluding Ge doping, high chemical homogeneity, a uniform microstructure, and a high degree of atomic order. These factors are all achieved through the rapid crystallization of melt-spun small-sized ribbons. Additionally, the ribbon geometry offers practical advantages, such as a high surface-area-to-volume ratio, which facilitates efficient heat transfer and can enhance the performance of laminate-based active magnetic regenerator (AMR) cycles in cooling devices.<sup>[12,13]</sup> In summary, the combination of a significant magnetocaloric effect in moderate magnetic fields, operation at near-room temperature, and geometric advantages of the ribbon form make these Ge-doped Ni–Co–Mn–Sn alloys highly attractive for compact and efficient solid-state cooling systems.

For practical magnetic refrigeration applications, it is particularly important to evaluate the relative cooling power (RCP) under moderate magnetic fields. RCP is estimated using the expression:

$$RCP = \Delta S_{150}^M \times \delta T_{FWHM} \quad (3)$$

where  $\Delta S_{150}^M$  is the maximum magnetic entropy change and  $\delta T_{FWHM}$  is the full width at half maximum of  $\Delta S_{150}$  curve at a field change of 2 T. The RCP values of our ribbons are found to be 148.5 J kg<sup>-1</sup> for SnGe1, 90.1 J kg<sup>-1</sup> for SnGe2, and 91.5 J kg<sup>-1</sup> for SnGe3 in this field. This performance is comparable to, or even better than, many other magnetocaloric materials such as Ni–Mn–based Heusler alloys and manganites reported in the literature.<sup>[70–72]</sup> Nevertheless, these values remain below those of Gd-based compounds, which typically exhibit RCP values on the order of  $\approx 200$  J kg<sup>-1</sup> under the same field change.<sup>[70]</sup>

It is noteworthy that in recent years Griffith et al.<sup>[73]</sup> introduced the temperature-averaged entropy change (TEC) as an additional figure of merit, which has since been widely employed to assess

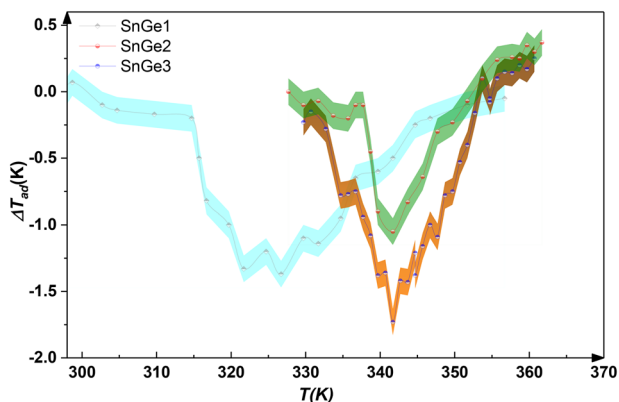


**Figure 9.** Adiabatic temperature change ( $\Delta T_{ad}$ ) as a function of temperature for SnGe1, SnGe2, and SnGe3 ribbons under a magnetic field change of 1.96 T. The shaded area around the data points represents the measurement uncertainty.

the effective performance of magnetocaloric materials. TEC expressed as following:

$$TEC(\Delta T_{lift}) = \frac{1}{\Delta T_{lift}} \left\{ \int_{T_{mid} - \frac{\Delta T_{lift}}{2}}^{T_{mid} + \frac{\Delta T_{lift}}{2}} \Delta S_{iso}(T)_{\Delta H} dT \right\} \quad (4)$$

where  $\Delta T_{lift}$  is a temperature range, and  $T_{mid}$  is the central temperature in which the TEC ( $\Delta T_{lift}$ ) reaches the maximum value for a given  $\Delta T_{lift}$ . For  $\Delta T_{lift} = 10$  K under a field change of 2 T, the TEC(10) values for SnGe1, SnGe2, and SnGe3 were found to be 12.1, 9.8, and 8.6 J kg<sup>-1</sup> K, respectively. These values are comparable to, and in some cases surpass, those of other well-studied magnetocaloric systems including manganites and Heusler alloys,<sup>[73–77]</sup> while exceeding the performance of state-of-the-art Gd-based materials at the same field change.<sup>[70]</sup>

The results of the direct measurements of  $\Delta T_{ad}$  under a magnetic field change of 1.96 T are shown in **Figure 9**. To minimize the effects of a thermal history, a discontinuous heating protocol was employed.<sup>[23]</sup> Among the series, the SnGe2 ribbon exhibited the largest  $\Delta T_{ad}$ , reaching  $\approx 1.8$  K. The observed trend in peak  $\Delta T_{ad}$  values (SnGe2 > SnGe3 > SnGe1) correlates well with the previously discussed trend in  $\Delta S_{iso}$  under 2T field, where SnGe2 also exhibited the most significant MCE. These consistent outcomes demonstrate that the intermediate Ge content in SnGe2 is optimal to maximize the magnitude of the magnetocaloric effect.

#### 4. Conclusion

In this study, we found that the martensitic transformation and magnetocaloric characteristics of the Ni<sub>42</sub>Co<sub>8</sub>Mn<sub>39</sub>Sn<sub>11-x</sub>Ge<sub>x</sub> ( $x = 1, 2, 3$ ) Heusler-type thin ribbons were significantly affected by the addition of Ge and the specific microstructure that develops as a result of the melt-spinning process. The substitution of Sn with Ge influences the MT temperatures and the thermal hysteresis of the transformation. The high chemical homogeneity and fine uniform microstructure of the ribbons, formed as a result of rapid solidification, are crucial for enhancing the magnetocaloric response. That is due to the high steepness of the trans-

formation front, which causes an increase in the proportion of the martensitic phase that undergoes a magnetic field-induced reverse MT. This, in turn, results in more efficient cooling of the ribbon at lower magnetic field. Among the compositions studied, the SnGe2 alloy ( $x = 2$ ) showed the highest magnetic field induced adiabatic temperature change and isothermal entropy variation. This suggests that a moderate Ge substitution can lead to an optimal balance between magnetization change and transformation entropy, effectively addressing the intrinsic trade-off often encountered in Heusler-type MSMA exhibiting inverse magnetocaloric effect. Furthermore, SnGe2 ribbon has shown the lowest MT hysteresis which is a result of the improved geometric compatibility between the austenitic and martensitic crystal lattices. Our highly homogeneous small-size ribbons demonstrate magnetocaloric responses that are comparable to those of bulk Ni-Mn-based MSMA, while outperforming previously reported ribbon counterparts in this alloy category. In summary, these findings demonstrate that strategic compositional adjustments in combination with melt-spinning processing result in the production of magnetocaloric ribbons that not only match the performance of bulk materials but also provide inherent benefits for microscale solid-state refrigeration systems.

#### Supporting Information

Supporting Information is available from the Wiley Online Library or from the author.

#### Acknowledgements

We acknowledge funding from the Alexander von Humboldt Foundation and Baden-Württemberg stiftung. Financial support from the Basque Government Department of Education (projects KK-2024/00048 and KK-2025/00034), the grant PID2022-138256NA-C22 funded by MCIN/AEI/10.13039/501100011033 and the European Space Agency through grant 4000148229/2025/NL/GLC (WISH Project) is also gratefully acknowledged. A.G. Varzaneh thanks SGiker services for their technical support and extends special thanks to Dr. Aitor Larranaga for conducting the XRD measurements. B. Aslibeiki and T. Sarkar gratefully acknowledge funding from Stiftelsen Olle Engkvist Byggmästare (grant number 214-0346) and the Swedish Research Council (grant number 2021-03675).

Open access funding enabled and organized by Projekt DEAL.

#### Conflict of Interest

The authors declare no conflict of interest.

#### Data Availability Statement

The data that support the findings of this study are available from the corresponding author upon reasonable request.

#### Keywords

magnetocaloric effect, martensitic transformation, Ni–Co–Mn–Sn–Ge ribbons, thermal hysteresis

Received: September 10, 2025  
Published online: November 19, 2025

- [1] T. Gottschall, K. P. Skokov, D. Benke, M. E. Gruner, O. Gutfleisch, *Phys. Rev. B* **2016**, *93*, 184431.
- [2] L. Pfeuffer, A. Gràcia-Condal, T. Gottschall, D. Koch, T. Faske, E. Bruder, J. Lemke, A. Taubel, S. Ener, F. Scheibel, K. Durst, K. P. Skokov, L. Mañosa, A. Planes, O. Gutfleisch, *Acta Mater.* **2021**, *217*, 117157.
- [3] J. Liu, T. Gottschall, K. P. Skokov, J. D. Moore, O. Gutfleisch, *Nat. Mater.* **2012**, *11*, 620.
- [4] M. Norouzi-Inallu, A. Ghotbi Varzaneh, P. Kameli, J. Xu, K. Ullakko, V. Chernenko, H. Hosoda, D. Salazar, *Intermetallics* **2024**, *165*, 108152.
- [5] X. Zhang, H. Zhang, M. Qian, L. Geng, *Sci. Rep.* **2018**, *8*, 8235.
- [6] S. K. Sarkar, P. Babu, V. Sharma, S. Kaushik, S. Goswami, M. Manekar, *Acta Mater.* **2024**, *276*, 120126.
- [7] P. Entel, M. E. Gruner, M. Acet, A. Çakir, R. Arróyave, T. Duong, S. Sahoo, S. Fähler, V. V. Sokolovskiy, *Energy Technol.* **2018**, *6*, 1478.
- [8] H. Xuan, P. Han, D. Wang, Y. Du, *J. Alloys Compd.* **2014**, *582*, 369.
- [9] W. Maziarz, P. Czaja, A. Wójcik, J. Dutkiewicz, J. Przewoźnik, E. Cesari, *Mater. Today: Proc.* **2015**, *2*, S523.
- [10] X. Zhao, X. Ning, C. W. Shih, M. Tong, W. C. Chang, W. Liu, Z. Zhang, *IEEE Trans. Magn.* **2013**, *50*, 1.
- [11] Z. D. Han, D. H. Wang, C. L. Zhang, H. C. Xuan, J. R. Zhang, B. X. Gu, Y. W. Du, *Mater. Sci. Eng., B* **2009**, *157*, 40.
- [12] K. A. Gschneidner, V. Pecharsky, A. Tsokol, *Rep. Prog. Phys.* **2005**, *68*, 1479.
- [13] S. C. Ma, C. W. Shih, J. Liu, J. H. Yuan, S. Y. Lee, Y. I. Lee, H. W. Chang, W. C. Chang, *Acta Mater.* **2015**, *90*, 292.
- [14] C. O. Aguilar-Ortiz, D. Soto-Parra, P. Álvarez-Alonso, P. Lázpita, D. Salazar, P. O. Castillo-Villa, H. Flores-Zúñiga, V. A. Chernenko, *Acta Mater.* **2016**, *107*, 9.
- [15] P. Devi, M. Ghorbani Zavareh, C. S. Mejía, K. Hofmann, B. Albert, C. Felser, M. Nicklas, S. Singh, *Phys. Rev. Mater.* **2018**, *2*, 122401.
- [16] K. Bhattacharya, *Microstructure and phase transition*, Springer, Berlin **1993**, pp. 1–25.
- [17] P. Álvarez-Alonso, J. López-García, G. Daniel-Perez, D. Salazar, P. Lázpita, J. P. Camarillo, H. Flores-Zúñiga, D. Rios-Jara, J. L. Sánchez-Llamazares, V. A. Chernenko, *Key Eng. Mater.* **2015**, *644*, 215.
- [18] S. Samanta, S. Chatterjee, J. Sinha, K. Mandal, *Phys. Rev. Mater.* **2023**, *7*, 084406.
- [19] T. Chabri, A. Ghosh, S. Nair, A. Awasthi, A. Venimadhav, T. Nath, *J. Phys. D: Appl. Phys.* **2018**, *51*, 195001.
- [20] D. Goswami, G. Potnis, S. Chattopadhyay, J. Das, *J. Alloys Compd.* **2022**, *917*, 165490.
- [21] P. Devi, C. S. Mejía, L. Caron, S. Singh, M. Nicklas, C. Felser, *Phys. Rev. Mater.* **2019**, *3*, 122401.
- [22] Z. Li, J. Yang, D. Li, Z. Li, B. Yang, H. Yan, C. F. Sánchez-Valdés, J. L. S. Llamazares, Y. Zhang, C. Esling, X. Zhao, L. Zuo, *Adv. Electron. Mater.* **2019**, *5*, 1800845.
- [23] C. O. Aguilar-Ortiz, J. P. Camarillo-García, J. Vergara, P. Álvarez-Alonso, D. Salazar, V. A. Chernenko, H. Flores-Zúñiga, *J. Alloys Compd.* **2018**, *748*, 464.
- [24] A. Wójcik, W. Maziarz, M. Szczerba, M. Kowalczyk, E. Cesari, J. Dutkiewicz, *Intermetallics* **2018**, *100*, 88.
- [25] S. Venkatesan, E. M. Abhinav, N. P. Kumar, S. Kavita, M. M. Raja, R. Parasuraman, D. M. Kandhasamy, S. Perumal, *ACS Appl. Energy Mater.* **2022**, *5*, 15959.
- [26] S. Ghosh, S. Sangwan, S. Mandal, S. Datta, M. Kar, P. Singh, T. K. Nath, *J. Magn. Magn. Mater.* **2022**, *562*, 169797.
- [27] O. Gutfleisch, T. Gottschall, M. Fries, D. Benke, I. Radulov, K. P. Skokov, H. Wende, M. Gruner, M. Acet, P. Entel, M. Farle, *Philos. Trans. R. Soc., A* **2016**, *374*, 20150308.
- [28] A. Taubel, T. Gottschall, M. Fries, S. Riegg, C. Soon, K. P. Skokov, O. Gutfleisch, *Phys. Status Solidi* **2018**, *255*, 1700331.
- [29] H. Sepehri-Amin, A. Taubel, T. Ohkubo, K. Skokov, O. Gutfleisch, K. Hono, *Acta Mater.* **2018**, *147*, 342.
- [30] B. Rodríguez-Crespo, N. A. Río-López, P. Lázpita, S. Ceballos, M. Ríos, D. Domenech, J. A. Rodríguez-Velamazán, J. López-García, V. Chernenko, J. M. Porro, D. Salazar, *Mater. Des.* **2024**, *245*, 113279.
- [31] A. M. Chirkova, K. P. Skokov, Y. Skourski, F. Scheibel, A. Y. Karpenkov, A. S. Volegov, N. V. Baranov, K. Nielsch, L. Schultz, K.-H. Müller, T. G. Woodcock, O. Gutfleisch, *Phys. Rev. Mater.* **2021**, *5*, 064412.
- [32] F. Scheibel, N. Shayanfar, L. Pfeuffer, T. Gottschall, S. Dittrich, A. Taubel, A. Aubert, I. Radulov, K. P. Skokov, O. Gutfleisch, *J. Appl. Phys.* **2025**, *137*, 014901.
- [33] A. Wójcik, W. Maziarz, M. J. Szczerba, M. Sikora, A. Żywczak, C. O. Aguilar-Ortiz, P. Álvarez-Alonso, E. Villa, H. Flores-Zúñiga, E. Cesari, J. Dutkiewicz, V. A. Chernenko, *J. Alloys Compd.* **2017**, *721*, 172.
- [34] W. Ito, M. Nagasako, R. Umetsu, R. Kainuma, T. Kanomata, K. Ishida, *Appl. Phys. Lett.* **2008**, *93*, 232503.
- [35] A. Wójcik, W. Maziarz, M. J. Szczerba, M. Sikora, J. Dutkiewicz, E. Cesari, *Mater. Sci. Eng., B* **2016**, *209*, 23.
- [36] W. Ito, Y. Imano, R. Kainuma, Y. Sutou, K. Oikawa, K. Ishida, *Metall. Mater. Trans. A* **2007**, *38*, 759.
- [37] A. M. G. Carvalho, A. Coelho, P. Von Ranke, C. Alves, *J. Alloys Compd.* **2011**, *509*, 3452.
- [38] M. N. Inallu, P. Kameli, A. G. Varzaneh, I. A. Sarsari, D. Salazar, I. Orue, V. A. Chernenko, *J. Phys. D: Appl. Phys.* **2019**, *52*, 235001.
- [39] A. G. Varzaneh, P. Kameli, I. A. Sarsari, M. G. Zavareh, C. S. Mejía, T. Amiri, Y. Skourski, J. L. Luo, T. H. Etsell, V. A. Chernenko, *Phys. Rev. B* **2020**, *101*, 134403.
- [40] P. Lázpita, A. Pérez-Checa, J. M. Barandiarán, E. L. Ammerlaan, U. Zeitler, V. Chernenko, *J. Alloys Compd.* **2021**, *874*, 159814.
- [41] S. Pandey, A. Quetz, A. Aryal, I. Dubenko, D. Mazumdar, S. Stadler, N. Ali, *Magnetochemistry* **2017**, *3*, 3.
- [42] C. L. Zhang, W. Q. Zou, H. C. Xuan, Z. D. Han, D. H. Wang, B. X. Gu, Y. W. Du, *J. Phys. D: Appl. Phys.* **2007**, *40*, 7287.
- [43] L. Wang, Z. Li, J. Yang, B. Yang, X. Zhao, L. Zuo, *Intermetallics* **2020**, *125*, 106888.
- [44] X.-M. Huang, Y. Zhao, H. L. Yan, N. Jia, B. Yang, Z. Li, Y. Zhang, C. Esling, X. Zhao, L. Zuo, *J. Alloys Compd.* **2021**, *889*, 161652.
- [45] L. Yang, H. Zhang, F. Hu, J. Sun, L. Pan, B. Shen, *J. Alloys Compd.* **2014**, *588*, 46.
- [46] F. Chen, J. L. Sánchez Llamazares, C. F. Sánchez-Valdés, F. Chen, Z. Li, Y. X. Tong, L. Li, *J. Alloys Compd.* **2020**, *825*, 154053.
- [47] Y. Qu, A. Gràcia-Condal, L. Mañosa, A. Planes, D. Cong, Z. Nie, Y. Ren, Y. Wang, *Acta Mater.* **2019**, *177*, 46.
- [48] J. Ouyang, Y. Tian, H. Xiao, Y. Zhang, *Mater. Chem. Phys.* **2021**, *273*, 125150.
- [49] T. Krenke, E. Duman, M. Acet, E. F. Wassermann, X. Moya, L. Mañosa, A. Planes, *Nat. Mater.* **2005**, *4*, 450.
- [50] V. Khovaylo, K. P. Skokov, O. Gutfleisch, H. Miki, T. Takagi, T. Kanomata, V. V. Koledov, V. G. Shavrov, G. Wang, E. Palacios, J. Bartolomé, R. Burriel, *Phys. Rev. B: Condens. Matter Mater. Phys.* **2010**, *81*, 214406.
- [51] P. Czaja, W. Maziarz, J. Przewoźnik, C. Kapusta, L. Hawelek, A. Chrobak, P. Drzymala, M. Fitta, A. Kolano-Burian, *J. Magn. Magn. Mater.* **2014**, *358*, 142.
- [52] W. Wang, H. Li, J. Ren, J. Fu, Q. Zhai, Z. Luo, H. Zheng, *J. Magn. Magn. Mater.* **2015**, *374*, 153.
- [53] Y. Yang, Z. Li, C. F. Sánchez-Valdés, J. L. Sánchez Llamazares, B. Yang, Y. Zhang, C. Esling, X. Zhao, L. Zuo, *J. Appl. Phys.* **2020**, *128*, 055110.
- [54] Z. Li, Y. Jiang, Z. Li, C. F. Sánchez Valdés, J. L. Sánchez Llamazares, B. Yang, Y. Zhang, C. Esling, X. Zhao, L. Zuo, *IUCrj* **2018**, *5*, 54.
- [55] I. Babita, S. Patil, S. Ram, *J. Phys. D: Appl. Phys.* **2010**, *43*, 205002.
- [56] Y. Yang, Z. Li, Z. Li, J. Yang, B. Yang, Y. Dong, H. Yan, Y. Zhang, C. Esling, X. Zhao, L. Zuo, *Crystals* **2017**, *7*, 289.
- [57] F. Chen, J. S. Llamazares, C. Sánchez-Valdés, P. Müllner, Y. Tong, L. Li, *J. Magn. Magn. Mater.* **2023**, *579*, 170900.

- [58] N. H. Dung, Z. Q. Ou, L. Caron, L. Zhang, D. T. C. Thanh, G. A. de Wijs, R. A. de Groot, K. H. J. Buschow, E. Brück, *Adv. Energy Mater.* **2011**, *1*, 1215.
- [59] V. K. Pecharsky, K. A. Gschneidner Jr., *Phys. Rev. Lett.* **1997**, *78*, 4494.
- [60] O. Tegus, E. Brück, K. Buschow, F. De Boer, *Nature* **2002**, *415*, 150.
- [61] S. Nikitin, G. Myalikgulyev, A. Tishin, M. Annaorazov, K. Asatryan, A. Tyurin, *Phys. Lett. A* **1990**, *148*, 363.
- [62] A. Fujita, S. Fujieda, Y. Hasegawa, K. Fukamichi, *Phys. Rev. B* **2003**, *67*, 104416.
- [63] H. N. Bez, A. K. Pathak, A. Biswas, N. Zarkevich, V. Balema, Y. Mudryk, D. D. Johnson, V. K. Pecharsky, *Acta Mater.* **2019**, *173*, 225.
- [64] B. Podmiljsak, P. McGuinness, N. Mattern, H. Ehrenberg, S. Kobe, *IEEE Trans. Magn.* **2009**, *45*, 4364.
- [65] T. Ho, T. Manh, N. Dang, C. Jung, B. Lee, T. Thanh, *J. Appl. Phys.* **2015**, *118*, 143902.
- [66] R. Thaljaoui, W. Boujelben, M. Pekala, K. Pekala, J. Antonowicz, J.-F. Fagnard, P. Vanderbemden, S. Dabrowska, J. Mucha, *J. Alloys Compd.* **2014**, *611*, 427.
- [67] X. Tan, P. Chai, C. M. Thompson, M. Shatruk, *J. Am. Chem. Soc.* **2013**, *135*, 9553.
- [68] C. F. Sánchez-Valdés, P. J. Ibarra-Gaytán, J. L. Sánchez Llamazares, M. Ávalos-Borja, P. Álvarez-Alonso, P. Gorria, J. A. Blanco, *Appl. Phys. Lett.* **2014**, *104*, 212401.
- [69] M. d. L. Arreguín-Hernández, A. Dzubinska, M. Reiffers, J. Llamazares, C. F. Sánchez-Valdés, R. Varga, *AIP Adv.* **2023**, *13*, 025336.
- [70] T. Gottschall, K. P. Skokov, M. Fries, A. Taubel, I. Radulov, F. Scheibel, D. Benke, S. Riegg, O. Gutfleisch, *Adv. Energy Mater.* **2019**, *9*, 1901322.
- [71] P. Z. Z. Nehan, B. Kurniawan, D. R. Munazat, O. Vitayaya, M. Naibaho, T. Sudiro, M. T. E. Manawan, D. Darminto, H. Nojiri, *J. Alloys Comp.* **2025**, *1020*, 179467.
- [72] P. Z. Z. Nehan, O. Vitayaya, D. R. Munazat, M. T. Manawan, D. Darminto, B. Kurniawan, *Phys. Chem. Chem. Phys.* **2024**, *26*, 14476.
- [73] L. Griffith, Y. Mudryk, J. Slaughter, V. Pecharsky, *J. Appl. Phys.* **2018**, *123*, 034902.
- [74] A. Kumar, I. Hussain, S. Khan, B. H. Koo, *J. Alloys Comp.* **2020**, *845*, 156218.
- [75] Y. Li, Y. Pan, *Mater. Lett.* **2024**, *376*, 137281.
- [76] X. Wang, Z. Ma, H. Wang, L. Li, *J. Alloys Comp.* **2021**, *883*, 160890.
- [77] B. Ge, Y. Liu, Z. Liu, X. Si, X. Luo, Y. Liu, *Intermetallics* **2024**, *171*, 108338.